Iranian Journal of Materials Forming 13 (2) (2026) 23-34

IJMF

Online ISSN: 2383-0042

Iranian Journal of Materials Forming

Journal Homepage: http://ijmf.shirazu.ac.ir

Research Article

Dual-Intermetallic FeCoNiSi High-Entropy Alloy Fabricated by Arc Melting: Insights into Deformation Behavior and Corrosion Resistance

Mikaeel Shirali, Khalil Gheisari [*], Mohsen Reihanian [†] and Javid Naseri

Department of Materials Science and Engineering, Faculty of Engineering, Shahid Chamran University of Ahvaz, Ahvaz, Iran

ARTICLE INFO

Article history:

Received: 14 October 2025
Reviewed: 12 November 2025
Revised: 14 November 2025
Accepted: 18 November 2025

Keywords:

FeCoNiSi high-entropy alloy
Arc melting
Dynamic recrystallization
Intermetallic phases
Corrosion resistance

Please cite this article as:

Shirali, M., Gheisari, K., Reihanian, M., & Naseri, J. (2026). Dual-intermetallic FeCoNiSi high-entropy alloy fabricated by arc melting: insights into deformation behavior and corrosion resistance. *Iranian Journal of Materials Forming*, *13*(2), 23-34. https://doi.org/10.22099/IJMF.2025.54549.1357

ABSTRACT

This study investigates a FeCoNiSi high-entropy alloy (HEA) produced via vacuum arc melting. The alloy exhibits a distinct dual-intermetallic microstructure, comprising orthorhombic Ni_2Si-type and cubic Fe_4Si_4-type phases, unlike the predominantly single-phase solid-solution structures reported for similar FeCoNi-based systems. Hot compression tests performed from 500–800 °C revealed a transition from brittle to ductile deformation, with dynamic recrystallization (DRX) occurring at higher temperatures. Avrami analysis yielded exponents of $n = 1.74$ (at 700 °C) and $n = 3.41$ (at 800 °C), indicating that the DRX mechanism depends on temperature. Electrochemical tests in 3.5 wt.% NaCl confirmed excellent corrosion resistance, evidenced by a low corrosion current density and spontaneous passivation. These results demonstrate the potential of FeCoNiSi HEAs for applications in high-temperature and corrosive environments.

1. Introduction

High- and medium-entropy alloys (HEAs/MEAs) have emerged as a new class of metallic materials characterized by multiple principal elements and high configurational entropy [1]. In contrast to conventional alloys that rely on one or two principal components, HEAs/MEAs are intentionally designed to favor the formation of simple solid-solution phases such as face-centered cubic (FCC), body-centered cubic (BCC), or

---

[*] Corresponding author
E-mail address: khalil.gheisari@yahoo.com (K. Gheisari)

[†] Corresponding author
E-mail address: m.reihanian@scu.ac.ir (M. Reihanian)
https://doi.org/10.22099/IJMF.2025.54549.1357

hexagonal close-packed (HCP) structures, rather than complex intermetallic compounds. This design philosophy results in exceptional combinations of mechanical strength, ductility, corrosion resistance, and thermal stability [2]. The distinction between HEAs and MEAs can be made according to their configurational entropy (ΔS). Generally, alloys with $\Delta S \geq 1.5R$ are classified as high-entropy alloys (HEAs), those with $1.5R > \Delta S \geq R$ as medium-entropy alloys (MEAs), and those with $\Delta S < 1.5R$ as low-entropy alloys (LEAs) [3, 4]. Based on this definition, the configurational entropy of the FeCoNiSi alloy in this study is approximately 1.39R, which places it near the MEA–HEA boundary. Thus, it may be more accurately described as a medium-to-high-entropy alloy. It should be noted, however, that an alternative and widely accepted compositional definition classifies HEAs as alloys containing at least four or five principal elements, each within 5–35 at.% [3, 4]. Under this convention, several quaternary or quinary equiatomic alloys are also referred to as HEAs, despite configurational entropies below 1.5R [5]. Therefore, the boundary between HEA and MEA classifications should be regarded as a continuum rather than a strict threshold, as alloy behavior depends on both entropy and enthalpic interactions.

The FeCoNiSi-based alloys have attracted significant interest due to their balanced mechanical and magnetic properties [6-11]. The inclusion of ferromagnetic elements (Fe, Co, Ni) and the metalloid Si allows for the tuning of phase stability and microstructure, which can be optimized for specific applications. The addition of Si promotes the formation of either FCC or BCC phases depending on composition, which is critical for their advanced structural and functional performance. Various synthesis routes have been employed for the fabrication of HEAs/MEAs, including vacuum arc melting, induction melting, mechanical alloying followed by spark plasma sintering, additive manufacturing, and high-pressure solidification [12]. Among these, vacuum arc melting is one of the most reliable methods for producing homogeneous ingots with controlled compositions and microstructures. This study presents an investigation of a FeCoNiSi HEA alloy synthesized via arc melting, revealing the simultaneous formation of orthorhombic Ni_2Si-type and cubic Fe_4Si_4-type intermetallic phases.

Previous studies have primarily focused on the microstructural evolution and magnetic performance of FeCoNiSi-based high- and medium-entropy alloys under various processing conditions. Chang et al. [6, 7] reported that high-pressure solidification refined Ni-rich phases and enhanced magnetic properties, while Chen et al. [8] achieved a fine BCC lamellar structure with superior strength and magnetization through copper mold casting. Yang et al. [9] demonstrated that additive manufacturing produced a single-phase FCC structure with improved ductility, and Li et al. [10] showed that Si content and annealing temperature affected crystallinity and magnetic absorption behavior. Zhu et al. [11] further revealed that Si addition promotes Ni_3Si precipitation, increasing resistivity but reducing magnetization. Collectively, these works underscore the significant influence of processing and composition on the magnetic and structural properties of FeCoNiSi alloys.

However, despite these advances, limited attention has been given to the deformation mechanisms and dynamic recrystallization (DRX) behavior of FeCoNiSi alloys, particularly at elevated temperatures, and to their corrosion resistance in chloride environments. Addressing these gaps, the present study investigates the high-temperature deformation behavior, DRX kinetics, and electrochemical performance of an arc-melted FeCoNiSi alloy, providing new insights into the interplay between its dual-intermetallic microstructure and its multifunctional properties. It should be acknowledged that the present FeCoNiSi alloy exhibits a dual-intermetallic microstructure composed of orthorhombic Ni_2Si-type and cubic Fe_4Si_4-type phases rather than a single-phase solid solution typically associated with classical HEAs or MEAs. However, similar multiphase or intermetallic-dominated structures have been widely reported in multi-principal element alloy systems derived from the high-entropy design concept. Accordingly, the FeCoNiSi system in this study is described as a medium-to-high-entropy, multi-principal-element alloy containing ordered intermetallic phases, consistent with modern classification schemes used in the literature.

2. Materials and Method

An FeCoNiSi alloy was synthesized from high-purity elements (Fe, Co, Ni, Si) with each present at a 25 atomic percent concentration. The raw materials were first cleaned, then melted in a vacuum arc melting furnace under an argon atmosphere. To remove residual oxygen, a titanium getter was melted. The molten alloy was cast into a water-cooled copper mold, producing ingots. These ingots were remelted at least five times to ensure a homogeneous chemical composition and a uniform microstructure throughout the material.

Metallographic specimens were extracted from the solidified ingots and subjected to sequential grinding and polishing to prepare them for microstructural characterization. For microstructural observation, the polished samples were etched using an acidic solution of 50 mL of 37% HCl, 10 g of $CuSO_4$, and 50 mL of H_2O for 5-15s. The resulting microstructure and elemental composition were then analyzed using an optical microscope and a field emission scanning electron microscope (FESEM) equipped with energy dispersive spectroscopy (EDS). To determine the phase structure, X-ray diffraction (XRD) was performed using a Philips Xpert-MPD diffractometer with Cu-Kα radiation, acquiring data over a 2θ range of 30-100° with a step size of 0.05° and a counting time of 1s per step.

Cylindrical samples with a diameter of 3 mm and a height of 4 mm were prepared using the wire-cut method. The compression tests were performed using a SANTAM - STM150 device equipped with a furnace. The samples were subjected to compression at temperatures of 500 °C, 600 °C, 700 °C, and 800 °C. Before testing, the samples were held at the specified temperatures for 10 minutes to ensure thermal stability. The hot compression tests were carried out with a jaw movement speed of 0.24 mm/min, an initial strain rate of 0.001 s^{-1}, and up to a 50% reduction in sample height.

Electrochemical experiments, comprising potentiodynamic polarization and electrochemical impedance spectroscopy (EIS), were performed at ambient temperature utilizing a standard three-electrode configuration in a 3.5 wt.% NaCl solution with an Auto Lab, AUT 84091. The setup comprised a silver/silver chloride (Ag/AgCl) reference electrode, a platinum rod counter electrode, and a 1 cm^2 working electrode fabricated from the test samples. Prior to electrochemical testing, the open circuit potential (OCP) was observed for 1800 seconds to ensure stabilization. EIS measurements were subsequently conducted at the stabilized OCP, utilizing a frequency range of 10 kHz - 10 mHz and an amplitude of ±10 mV. The EIS data was analyzed using Zview software to model an equivalent circuit. Potentiodynamic polarization experiments were performed at a scan rate of 1 mV/s, across a potential range from -300 mV to +1000 mV relative to the OCP.

3. Results and Discussion

3.1. Microstructural characterization

Fig. 1 presents the XRD patterns of the synthesized FeCoNiSi alloy, revealing its multiphase crystallographic structure. The left panel shows the full XRD pattern from 30º to 85º, identifying the presence of two distinct phases. Peaks marked with blue stars correspond to an orthorhombic phase (Ni_2Si type, PDF No: 0779-050-00), while those with red stars belong to a cubic phase (Fe_4Si_4 type, PDF No: 1344-101-96). The sharp, high-intensity peaks for both phases confirm their significant formation and high crystallinity. To provide a clearer view of overlapping peaks, the right panel shows a magnified view of the 2θ range from 43º - 51º. This magnified section distinctly resolves characteristic reflections, including the orthorhombic (021), (220), (121), and (002) planes, and the cubic (012) and (112) planes. A prominent reflection at approximately $2\theta \approx 45.3°$ is likely due to the overlap of the cubic (012) and orthorhombic (121) peaks. This detailed analysis of both the full and magnified patterns confirms that the synthesized FeCoNiSi alloy is a multiphase material consisting of both orthorhombic and cubic phases.

As shown in Table 1, the FeCoNiSi alloy fabricated by arc melting develops a dendritic microstructure with Ni_2Si-type and Fe_4Si_4-type intermetallic phases, in contrast to earlier studies that mainly reported single-

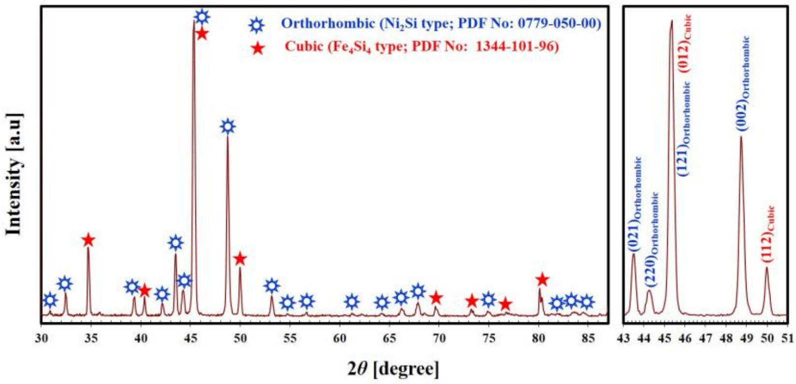

Fig. 1. XRD patterns of the synthesized FeCoNiSi alloy. The left panel shows the full scan, identifying orthorhombic (Ni_2Si type) and cubic (Fe_4Si_4 type) phases. The right panel provides a magnified view of key diffraction peaks.

Table 1. Comparison of the fabrication methods, alloy compositions, resulting microstructures, and identified phases of FeCoNiSi-based high/medium entropy alloys in the present study and previous works

Alloy	Fabrication Method	Phases Identified	Study
FeCoNiSi	Arc melting	Orthorhombic Ni_2Si-type and cubic Fe_4Si_4-type intermetallic phases	Present Work
FeCoNiSi	High-pressure solidification (0.1–7 GPa)	Ordered B2 phase (Ni, Si-rich); BCC matrix (Fe, Co-rich)	[6]
FeCoNiSi	High-pressure solidification	B2, BCC1, and BCC2 phases, varying with pressure; merging/disappearance of peaks	[7]
$Fe_{40}Co_{40}Ni_{10}Si_{10}$	Copper mold casting	Dominant BCC phase; minor FCC phase	[8]
$FeCoNiSi_{0.2}$	Additive manufacturing (laser-based)	Single FCC solid solution; peak shifts with Si content	[9]
$Fe_1Co_{0.8}Ni_1Si_x$ ($x = 0.5–0.7$)	Chemical reduction + annealing	Initially amorphous; transitions to FCC-FeCoNi(Si) solid solution with increasing annealing temp	[10]
$CoFeNiSi_x$ ($x = 0–1.0$)	Arc melting	FCC matrix; Ni_3Si precipitates form at higher Si content	[11]

phase FCC, BCC, or B2 structures formed through high-pressure solidification, rapid solidification, or additive manufacturing. This unique phase formation indicates a different solidification pathway and elemental partitioning during arc melting, which may contribute to improved mechanical strength and corrosion resistance, underscoring the critical role of processing in tailoring phase evolution and alloy performance.

Optical and SEM analyses of the arc-melted FeCoNiSi alloy reveal a distinct two-phase microstructure. At low and high magnification, optical micrographs (Figs. 2(a) and 2(b)) show elongated, dendritic bright regions embedded in a darker matrix, indicating a directional solidification pattern with clear phase boundaries and intergrowth features. Quantitative image analysis of the micrographs indicates that the average primary dendrite arm spacing (PDAS) is approximately 8–12 µm, while the secondary dendrite arm spacing (SDAS) ranges from 3–5 µm, reflecting a relatively fine dendritic morphology typical of alloys solidified by vacuum arc melting [13].

The BSE-SEM image (Fig. 2(c)) confirms a strong atomic number contrast between the bright and dark phases. The EDS microanalysis indicates that the bright and dark regions in the BSE-SEM image contain approximately 33.84 at.% and 49.72 at.% Si, respectively. These values are in good agreement with the nominal Si contents of the Ni_2Si (33.3 at.% Si) and Fe_4Si_4 (50 at.% Si) compounds, which were also detected based on the XRD patterns. However, the phase identification is derived from reference XRD data for the binary Ni–Si and Fe–Si systems.

In the present study, since the alloy contains multiple principal elements (Fe, Co, Ni, and Si), the stoichiometry of the detected intermetallics may deviate slightly from their ideal binary compositions. This deviation can be

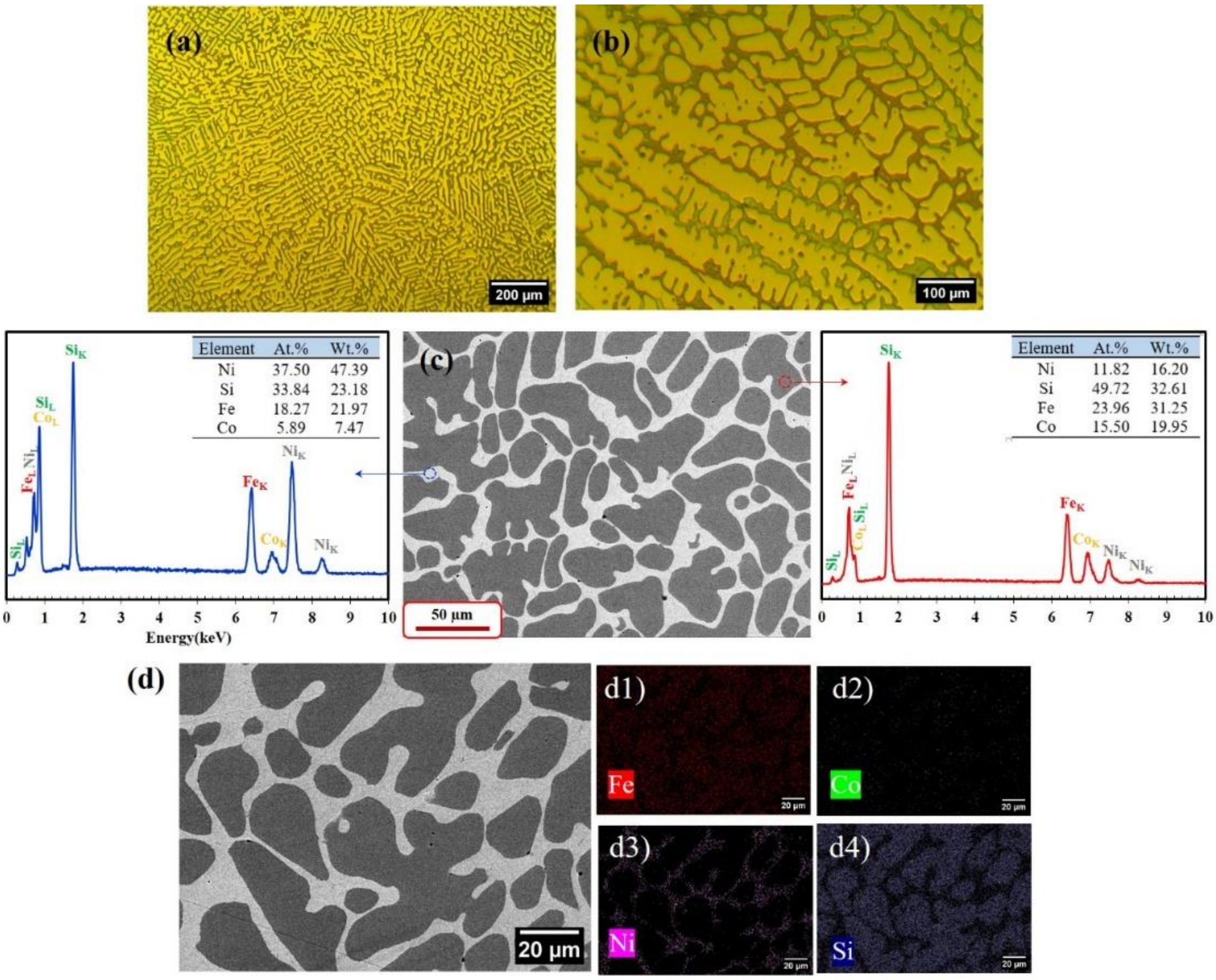

Element	At.%	Wt.%
Ni	37.50	47.39
Si	33.84	23.18
Fe	18.27	21.97
Co	5.89	7.47

Element	At.%	Wt.%
Ni	11.82	16.20
Si	49.72	32.61
Fe	23.96	31.25
Co	15.50	19.95

Fig. 2. (a, b) Optical micrographs revealing the microstructure of the synthesized FeCoNiSi alloy at different magnifications, (c) backscattered electron (BSE) SEM image with corresponding EDS point analyses and elemental compositions, (d) SEM image and elemental maps illustrating the distribution of Fe, Co, Ni, and Si.

attributed to the partial substitution (solid solubility) of Fe and Co atoms into the Ni_2Si- and Fe_4Si_4-type crystal lattices while preserving their overall crystallographic structures. As a result, although crystalline structures similar to Ni_2Si and Fe_4Si_4 have been identified, their chemical compositions are somewhat modified. Interestingly, both phases still contain Si concentrations that closely match those of the ideal Ni_2Si and Fe_4Si_4 compounds. For this reason, the phases are referred to as Ni_2Si-type and Fe_4Si_4-type, emphasizing that they retain the same orthorhombic and cubic crystal structures as their reference intermetallics but exhibit compositional modification arising from elemental substitution effects.

Quantitative analysis shows the bright phase occupies approximately 34.2% of the area. These results, supported by EDS and XRD, associate the bright phase with the orthorhombic Ni_2Si-type phase and the darker phase with the cubic Fe_4Si_4-type phase. Elemental mapping (Fig. 2(d)) visually confirms this partitioning, showing Ni concentrated in the bright regions, Fe and Co in the matrix, and Si present in both phases. This compositional segregation highlights the influence of arc melting on phase formation and underlines the microstructural basis for the alloy's mechanical and corrosion behavior.

3.2. Deformation behavior and kinetics of DRX

Fig. 3 shows the compressive stress-strain behavior of the FeCoNiSi medium-to-high-entropy alloy across various temperatures. The material exhibits a brittle-to-ductile transition with increasing temperature. At 500 °C and 600 °C, the alloy displays brittle failure, characterized by a sharp stress drop after reaching fracture stresses of around 650 MPa and 425 MPa, respectively. At higher temperatures, dynamic recrystallization (DRX) becomes active, promoting ductile deformation. At 700 °C, a distinct peak stress (~230 MPa) is followed by a steady-state flow, indicating DRX-induced softening. This effect is even more pronounced at 800 °C, where a lower peak stress (~200 MPa) leads to a stable, extended steady-state flow. These results confirm that DRX is a key mechanism responsible for significantly enhancing the alloy's ductility and workability at elevated temperatures. The brittle behaviour exhibited by the FeCoNiSi alloy at lower temperatures is attributed to the presence of dual intermetallic phases—namely, orthorhombic Ni_2Si-type and cubic Fe_4Si_4-type structures. The highly ordered atomic arrangements in these phases provide limited slip systems necessary for plastic deformation, thereby yielding high mechanical strength at the expense of ductility. At higher temperatures, however, dynamic recrystallization (DRX) and thermally activated processes refine grains and enhance dislocation mobility, enabling steady-state flow and ductile deformation that counteracts the alloy's inherent brittleness.

3.3. Avrami kinetics of DRX

Avrami's equation is used to describe recrystallization kinetics, typically for static recrystallization (SRX), where the recrystallized volume fraction (*X*) is modeled as a function of time using:

$$X = 1 - exp(-kt^n) \tag{1}$$

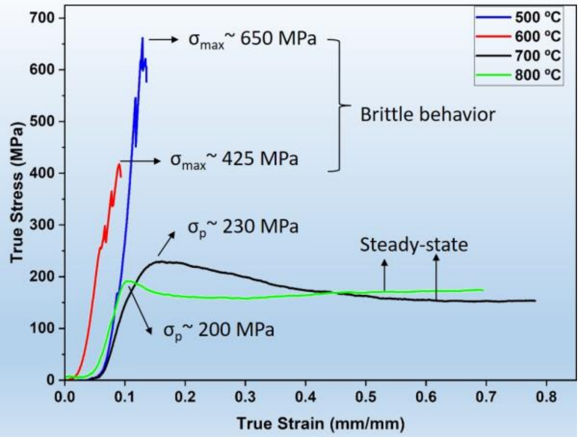

Fig. 3. Compressive true stress-strain curve of the FeCoNiSi alloy at various temperatures.

with *k* representing a material constant and *n* representing the Avrami exponent. For DRX, since direct measurement of *X* is difficult, fractional softening is used instead:

$$X = \frac{\Delta\sigma}{\sigma_{sat} - \sigma_{ss}} \tag{2}$$

where $\Delta\sigma$ represents the stress reduction due to DRX, σ_{sat} is the saturation stress from the DRV curve, and σ_{ss} is the steady-state stress from the DRX curve. DRX onset is defined by the critical stress σ_c and strain ε_c. The DRV curve, which cannot be directly measured due to overlapping DRX effects, is inferred from the work hardening behavior using the equation:

$$\sigma = [\sigma_{sat}^2 - (\sigma_{sat}^2 - \sigma_{\circ}^2)exp(-r\varepsilon)]^{1/2} \tag{3}$$

where *r* is the dynamic recovery rate and $\sigma_{\circ}$ is the yield stress. Differentiation of this expression leads to a linear relation:

$$\sigma\frac{d\sigma}{d\varepsilon} = 0.5r\sigma_{sat}^2 - 0.5r\sigma^2 \tag{4}$$

Key parameters like σ_p, $\sigma_{\circ}$, σ_c, σ_{sat} , and *r* are extracted from stress-strain and work hardening plots. The σ_p corresponds to the point where the work hardening rate $\theta = d\sigma/d\varepsilon$ reaches zero. The σ_{sat} is determined by extrapolating the linear portion of the θ-σ curve to $\theta = 0$, and the σ_c, indicating the onset of DRX, is identified as the point of inflection in the θ-σ plot. The dynamic recovery rate *r* is determined from the slope of the $\theta\sigma - \sigma^2$ plot, and the steady-state stress is extrapolated from the DRX curve beyond the peak.

Figs. 4(a) and (b) display work hardening rate (θ) versus flow stress (σ) plots, which are fundamental for characterizing DRV and DRX at 700 °C and 800 °C. These plots show initial work hardening (positive θ) followed by a decrease, reaching zero at the peak stress (σ_p). The saturation stress (σ_{sat}), where work hardening balances DRV, is determined by extrapolating the linear portion of the $\theta - \sigma$ curve to $\theta = 0$, while the critical stress (σ_c), indicating DRX initiation, is identified by a deviation from DRV behavior. Complementing this, Figs. 4(c) and (d) present $\theta\sigma - \sigma^2$ plots, which are used to infer the DRV curve and quantitatively determine the dynamic recovery rate (r) from the slope $m=-0.5r$. The observed slopes (m = −48.6 for 700 °C and m = −24.64 for 800 °C) highlight that temperature significantly influences the recovery rate, with higher temperatures yielding higher rates. Both sets of plots effectively differentiate deformation stages, allowing for a comprehensive analysis of DRX progression and the temperature's impact on the alloy's high-temperature mechanical behavior.

Figs. 5(a) and (b) display the linearized Avrami plots, $\ln[\ln(1/1-X)]$ versus $\ln t$, which are used to determine the Avrami exponent (n) for DRX at 700 °C and 800 °C, respectively. The Avrami exponent (n) increases from 1.74 at 700 °C to 3.41 at 800 °C, indicating a clear transition in the dominant recrystallization mechanism. At 700 °C, an n value close to 2 suggests that grain growth may be limited by internal barriers [14]. In contrast, the higher n value at 800 °C (≈3–4) reflects a shift toward continuous nucleation and three-dimensional grain growth [14], likely due to enhanced atomic mobility and dynamic recovery at elevated temperatures. This temperature-dependent evolution of n confirms that dynamic recrystallization (DRX) in the FeCoNiSi alloy becomes progressively dominated by continuous nucleation and growth processes as the deformation temperature increases.

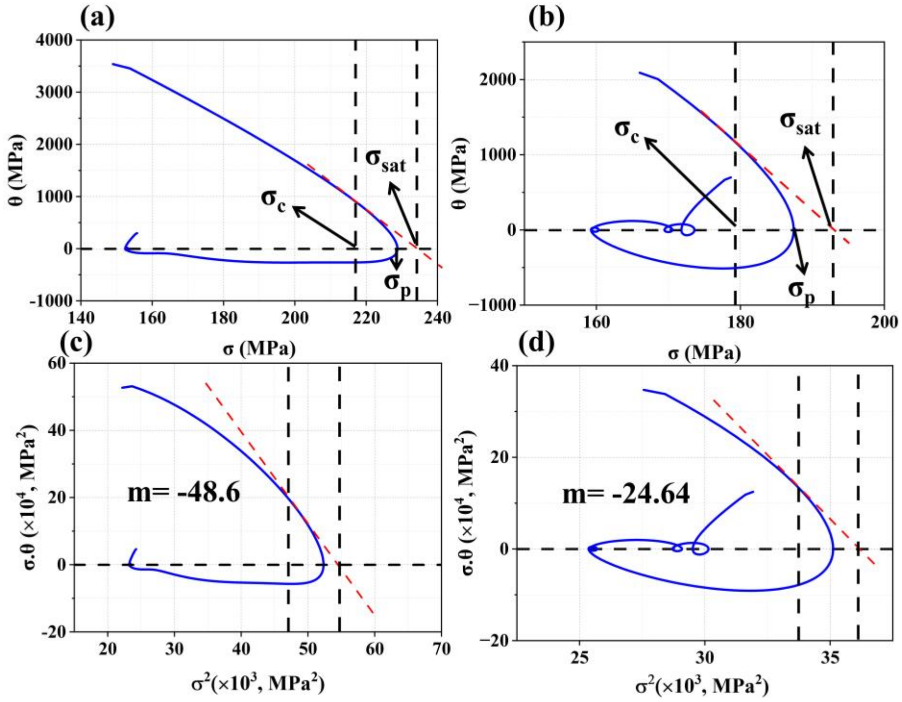

Fig. 4. Determination of Avrami kinetics for DRX in FeCoNiSi alloy. (a, b) θ-σ plots, (c, d) θσ-σ^2 plots for determining the dynamic recovery rate. (a) and (c) correspond to 700 °C, and (b) and (d) correspond to 800 °C.

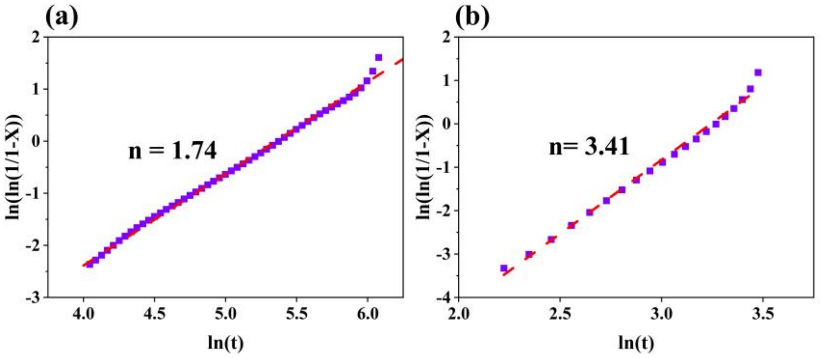

Fig. 5. $\ln[\ln(1/1-\mathrm{X})]$ vs. $\ln t$ plots at (a) 700 °C and (b) 800 °C for Avrami exponent.

3.4. Corrosion behavior

As shown in Fig. 6(a), the polarization curve of the FeCoNiSi alloy in a 3.5 wt.% NaCl solution at room temperature reveals the absence of a well-defined active-to-passive transition. Instead, the anodic branch exhibits semi-passive behavior, characterized by a gradual increase in current density within a specific potential range where passivation is presumed stable. This slight rise in current density suggests the formation of a passive film that limits further metal dissolution, indicative of spontaneous or self-passivating behavior in the chloride-containing environment. Eventually, the breakdown potential is reached, beyond which the current density increases sharply, signifying the failure of the passive film and the onset of pitting corrosion.

The corrosion potential (E_{corr}) of the FeCoNiSi alloy is approximately –355 mV (vs. Ag/AgCl), and the corrosion current density (i_{corr}) is determined to be 0.81 μA/cm² by extrapolating the cathodic Tafel region to its intersection with a horizontal line drawn at E_{corr}. These values reflect good general corrosion resistance, as lower i_{corr} values are typically associated with reduced corrosion rates. The pitting potential (E_b), observed at –124 mV (vs. Ag/AgCl), marks the onset of localized breakdown of the passive film. The passivation potential range (ΔE_p), calculated as $\Delta E_p = E_b - E_{corr}$, is therefore 231 mV. This relatively wide range suggests the presence of a moderately stable passive film. Given the spontaneous passivation behavior, the passivation current density in this system can be reasonably approximated by i_{corr}. The presence of a distinct passivation region, a well-defined breakdown potential, and a low corrosion current density collectively indicate that the FeCoNiSi alloy spontaneously forms a stable and protective passive layer, thereby exhibiting effective corrosion resistance in chloride-containing environments.

Figs. 6(b) and 6(c) display the electrochemical impedance spectroscopy (EIS) results for the FeCoNiSi alloy, presented as both a Nyquist plot (Fig. 6(b)) and a Bode-phase plot (Fig. 6(c)). Fig. 6(b) shows the Nyquist plot, where the imaginary part of the impedance (Z'') is plotted against the real part of the impedance (Z'). The observed data points are well-fitted by the solid green line, indicating a good agreement with the proposed equivalent circuit model. The inset of Fig. 6(b) shows the equivalent circuit used to simulate the alloy's electrochemical response, represented as: $Rs+[CPE_f \parallel (R_f + CPE_{dl} \parallel R_{ct})]$. In this circuit, R denotes resistance and CPE represents a constant phase element, used instead of an ideal capacitor to account for deviations from ideal dielectric behavior. Such deviations often arise from surface roughness, inhomogeneity, or localized current leakage [15]. These factors are particularly relevant for the FeCoNiSi alloy due to its heterogeneous dual-phase microstructure. Therefore, incorporating $CPEs$ yields a more physically meaningful model of the electrochemical interface and ensures a more accurate fit to the experimental data. The impedance of a CPE is calculated as follows [15]:

$$Z_{CPE} = \frac{1}{Q(\omega i)^n} \tag{5}$$

where Q is the CPE admittance, ω is the angular frequency, i is the imaginary unit ($i^2 = -1$), and n is an exponent ($0 < n \leq 1$) reflecting surface inhomogeneity. The fitted circuit parameters are: solution resistance R_s = 13.8 Ω, passive film resistance R_f = 4.1 Ω, and a surface film modeled by CPE_f with Q_f = 2.8 μF·cm^{-2}·s^{n-1} and n = 0.98. The electrochemical double layer is represented by CPE_{dl} with Q_{dl} = 9.6 μF·cm^{-2}·s^{n-1} and n = 0.83, in parallel with the charge transfer resistance R_{ct} = 51081 Ω. The model reflects a two-layer structure: the outer passive film characterized by R_f and CPE_f, and the electrochemical interface represented by R_{ct} and CPE_{dl}. The high R_{ct} value (51081 Ω) indicates substantial resistance to charge transfer at the alloy/electrolyte interface, reflecting very slow corrosion kinetics. This strongly implies that the FeCoNiSi alloy possesses excellent intrinsic corrosion resistance in the tested NaCl environment.

Fig. 6(c) presents the Bode plot, which complements the Nyquist plot by showing the logarithm of impedance magnitude (|Z|) and the phase angle (−Phase) as a function of the logarithm of frequency (log f). The Bode plot further confirms the presence of at least two time

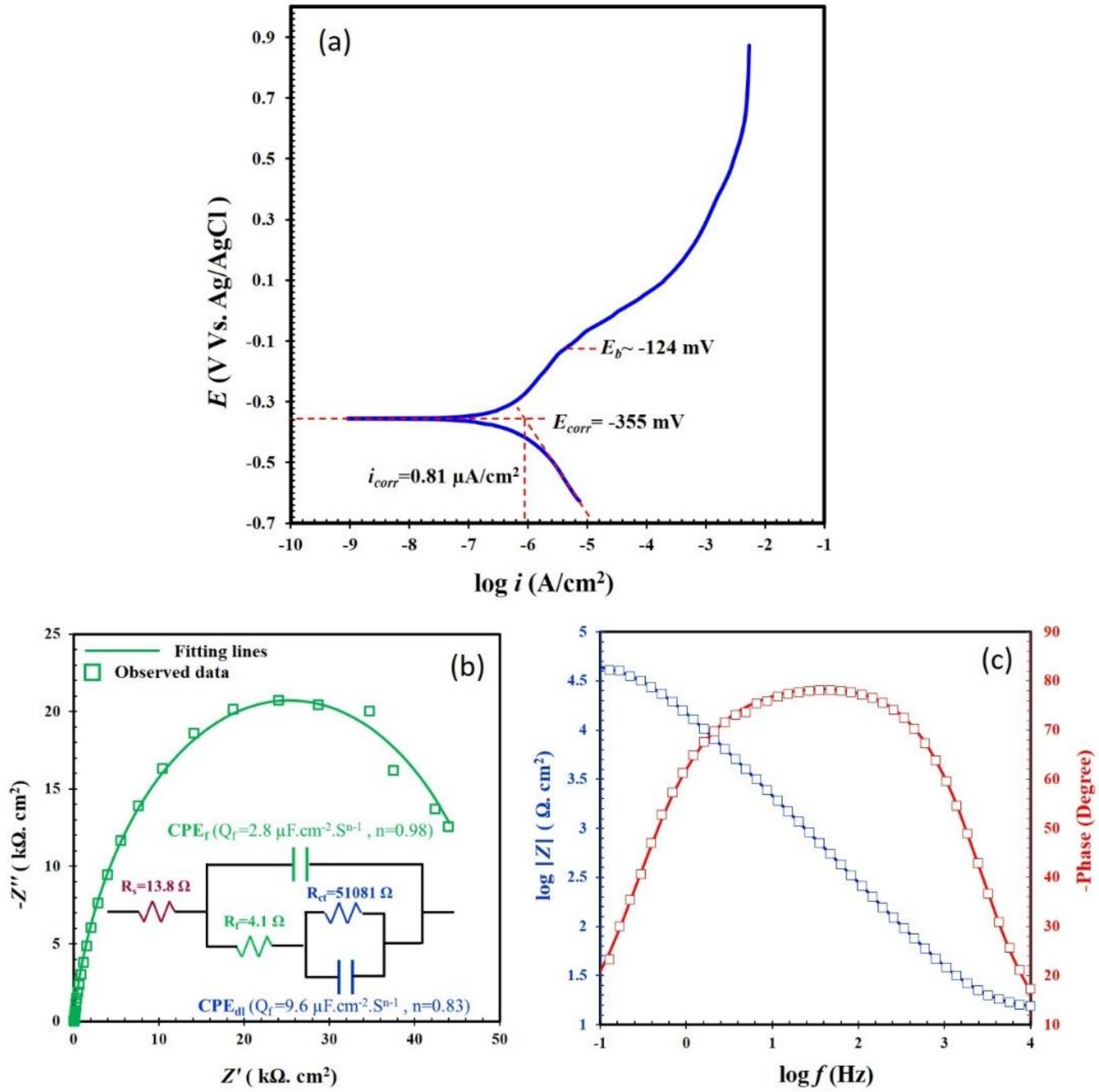

Fig. 6. (a) Potentiodynamic polarization curve of the FeCoNiSi alloy, (b) Nyquist plot and the fitted equivalent electrical circuit model with corresponding parameters, and (c) Bode plot.

constants, although they are closely spaced or overlapping. In the impedance magnitude plot (blue squares), two distinct plateaus or slope changes are observed, signifying different resistive and capacitive behaviors at various frequency ranges. At high frequencies, the impedance magnitude approaches the R_s. As frequency decreases, the impedance magnitude increases significantly, reflecting the combined resistance of the surface film and the charge transfer process.

The Bode-phase plot (red squares) in Fig. 6(c) reveals a broad and prominent peak in the mid-frequency range (10^1–10^3 Hz), where the phase angle reaches a maximum of approximately –78°. This behavior is characteristic of a semi-capacitive response, typically associated with the formation of a stable passive film on the alloy surface. The presence of a single, wide peak—rather than two distinct ones—suggests that the two electrochemical processes, namely the response of the passive film and the charge transfer process at the interface, are not fully resolved and exhibit overlapping time constants. The considerable height and broad width of this phase angle peak further imply that the passive film is both protective and stable. Additionally, the high impedance magnitude observed at low frequencies supports the conclusion that the FeCoNiSi alloy exhibits excellent resistance to corrosion under the test conditions.

A comparison between the corrosion behavior of the FeCoNiSi alloy and the FeCoNi alloy reported in the literature under the same 3.5 wt.% NaCl environment [16] clearly demonstrates the significant improvement achieved through Si addition. While the total resistance ($R_t = R_f + R_{corr}$) for FeCoNi is approximately 5 kΩ·cm², the corresponding value obtained in the present study is ~51 kΩ·cm², indicating an order-of-magnitude enhancement in corrosion resistance. This improvement is primarily attributed to the beneficial effect of Si in promoting the formation of a denser and more stable passive film. However, unlike traditional corrosion-resistant alloys, in which a single element may dominate passivation behavior, HEAs involve complex multi-element interactions. Thus, the synergistic contributions of Co, Ni, and Fe—combined with Si—must also be considered, reflecting the characteristic "cocktail effect" in HEAs.

A deeper understanding of the passivation chemistry could be further enriched by employing advanced surface-analysis techniques such as X-ray photoelectron spectroscopy (XPS). Such analyses would help determine whether the enhanced corrosion resistance is associated with the formation of a SiO_2-enriched passive film, the presence of mixed or complex oxides, or synergistic effect of Si in stabilizing other protective oxide species. For example, in AlCoCrFeNi HEAs, previous studies have shown that when the Si molar ratio is ≤ 0.2, the Cr^{3+}/Cr peak-area ratio increases with Si addition, indicating improved Cr-based passivation. At higher Si contents, however, the formation of Cr-containing silicides can hinder Cr passivation and reduce corrosion resistance [17].

Beyond the chemical effects of Si, microstructural evolution must also be considered. While FeCoNi typically exhibits a simple FCC solid-solution structure [13], the addition of Si in the present alloy promotes the formation of two complex intermetallic phases, leading to a dual-phase microstructure consisting of dendritic and interdendritic regions. Dual-phase alloys are generally more susceptible to micro-galvanic corrosion than single-phase systems [18], and previous studies likewise report that Si addition can induce dual-phase formation [19]. At high Si levels, this galvanic effect can dominate and reduce corrosion resistance [19, 20].

For instance, Yang et al. [19] reported improved corrosion resistance in $Al_{0.2}CoCrFe_{1.5}NiSi_{0.1}$ due to the suppression of surface-active sites at low Si levels, whereas excessive Si increased galvanic activity and reduced corrosion performance. Similarly, Shi et al. [20] observed that in $FeCrNiAl_{0.7}Cu_{0.3}Si_x$ HEAs, corrosion resistance increased up to Si = 0.3 due to the formation of a dense passive film, but decreased at higher Si contents because of intensified micro-galvanic coupling. Taken together, these findings indicate that the optimal Si content strongly depends on alloy composition and crystal structure. Considering this context, the substantial enhancement observed in the present FeCoNiSi alloy—compared with FeCoNi reported in the literature [13]—suggests that the Si concentration adopted in this study lies within an optimal range. Despite the presence of a dual-phase microstructure, the beneficial effects of Si on passive film formation and stability clearly dominate, resulting in the markedly improved corrosion resistance demonstrated in this work.

4. Conclusions

1. The alloy exhibits a two-phase microstructure consisting of an orthorhombic Ni_2Si-type phase and a cubic Fe_4Si_4-type phase, as confirmed by XRD and SEM/EDS analyses. Significant elemental partitioning is observed, with Ni and Si enriched in the bright phase and Fe and Co concentrated in the darker matrix phase.
2. Compression tests reveal a temperature-dependent transition from brittle to ductile behavior. At 700 °C and 800 °C, dynamic recrystallization (DRX) occurs, leading to flow softening and steady-state deformation, indicating enhanced ductility at elevated temperatures.
3. The kinetics of DRX were evaluated using Avrami analysis. The Avrami exponents determined were n = 1.74 at 700 °C and n = 3.41 at 800 °C, suggesting that the DRX

mechanism evolves with temperature due to changes in nucleation rates and grain growth behavior.

4. Electrochemical testing in 3.5 wt.% NaCl solution showed that the alloy forms a moderately stable passive film, with a low corrosion current density ($0.81\ \mu A/cm^2$) and a high charge transfer resistance ($51\ k\Omega$), demonstrating excellent resistance to general and localized corrosion.
5. The FeCoNiSi alloy combines high-temperature mechanical performance and corrosion resistance, making it a promising candidate for structural applications in aggressive environments. The insights into DRX behavior and microstructural evolution also provide valuable guidance for further processing and optimization of similar high-entropy alloys.

Authors' contributions

M. Shirali: Investigation

Kh. Gheisari: Supervision, Methodology

M. Reihanian: Supervision, Writing original draft, Writing - review & editing

J. Naseri: Formal analysis

Conflict of interest

The authors have no relevant financial or non-financial interests to disclose.

Data availability

The data will be made available upon request.

Funding

The founding of Shahid Chamran University of Ahvaz (Ahvaz, Iran) through grant number SCU.EM1403.375 is gratefully appreciated.

5. References

[1] Zhang, Y., Zuo, T. T., Tang, Z., Gao, M. C., Dahmen, K. A., Liaw, P. K., & Lu, Z. P. (2014). Microstructures and properties of high-entropy alloys. *Progress in Materials Science*, *61*, 1-93. https://doi.org/10.1016/j.pmatsci.2013.10.001

[2] Yeh, J. W. (2013). Alloy design strategies and future trends in high-entropy alloys. *JOM*, *65*, 1759-1771. https://doi.org/10.1007/s11837-013-0761-6

[3] Miracle, D. B., & Senkov, O. N. (2017). A critical review of high entropy alloys and related concepts. *Acta Materialia*, *122*, 448-511. https://doi.org/10.1016/j.actamat.2016.08.081

[4] Ye, Y., Wang, Q., Lu, J., Liu, C., & Yang, Y. (2016). High-entropy alloy: challenges and prospects. *Materials Today*, *19*(6), 349-362. https://doi.org/10.1016/j.mattod.2015.11.026

[5] Gao, M. C., Yeh, J. W., Liaw, P. K., & Zhang, Y. (2016). *High-entropy alloys: fundamentals and applications*. Springer.

[6] Chang, T., Zou, C., Zhu, D., Wang, X., Wei, Z., Wang, H., Fang, N., & Chen, J. (2022b). Second phases' distribution of FeCoNiSi high-entropy alloy solidified under high pressure and its effect on magnetic properties. *IEEE Transactions on Magnetics*, *59*(6), 1-7. https://doi.org/0.1109/TMAG.2022.3232722

[7] Chang, T., Zou, C., Zhu, D., Wang, X., Wei, Z., Wang, H., Fang, N., & Chen, J. (2022a). The evolution of microstructure, micromechanical and magnetic properties of FeCoNiSi alloys solidified under high pressure. *Materials Characterization*, *189*, 112009. https://doi.org/10.1016/j.matchar.2022.112009

[8] Chen, C., Fan, Y., Zhang, H., Hou, J., Zhang, W., Wei, P., Wang, W., Qin, J., Wei, R., & Wang, T. (2020). A novel Fe-Co-Ni-Si high entropy alloy with high yield strength, saturated magnetization and Curie temperature. *Materials Letters*, *281*, 128653. https://doi.org/10.1016/j.matlet.2020.128653

[9] Yang, Y., Liao, T., Jia, Y., Ding, G., Cao, J., Shang, X., Guo, Y., & Liu, Q. (2024). Additively manufactured FeCoNiSi0. 2 alloy with excellent soft magnetic and mechanical properties through texture engineering. *Journal of Materials Research and Technology*, *33*, 1910-1922. https://doi.org/10.1016/j.jmrt.2024.09.171

[10] Li, H., Li, H., Shen, Z., Zeng, S., Yang, F., Cai, Q., Xu, W., Wang, R., Luo, C., & Liu, Y. (2024). Investigation of the impact of non-magnetic Si element addition and heat treatment on the electromagnetic wave absorption properties of medium entropy FeCoNiSi alloy particles. *Powder Technology*, *446*, 120132. https://doi.org/10.1016/j.powtec.2024.120132

[11] Zuo, T., Li, R., Ren, X., & Zhang, Y. (2014). Effects of Al and Si addition on the structure and properties of CoFeNi equal atomic ratio alloy. *Journal of Magnetism and Magnetic Materials*, *371*, 60-68. https://doi.org/10.1016/j.jmmm.2014.07.023

[12] Kaushik, N., Meena, A., & Mali, H. S. (2022). High entropy alloy synthesis, characterisation, manufacturing & potential applications: a review. *Materials and*

Manufacturing Processes, *37*(10), 1085-1109. https://doi.org/10.1080/10426914.2021.2006223

[13] Chai, W., Lu, T., & Pan, Y. (2020). Corrosion behaviors of FeCoNiCrx (x= 0, 0.5, 1.0) multi-principal element alloys: Role of Cr-induced segregation. *Intermetallics*, *116*, 106654. https://doi.org/10.1016/j.intermet.2019.106654

[14] Humphreys, F. J., & Hatherly, M. (2012). *Recrystallization and Related Annealing Phenomena*. Elsevier Science.

[15] Heidari, Y., Gheisari, K., & Yeganeh, M. (2025). Effect of Cr content on the structure and corrosion properties of (FeCoNi)0.75Cu0.25-xCrx high entropy alloys in 1 M H2SO4. *Journal of Materials Research and Technology*, *35*, 5322-5335. https://doi.org/10.1016/j.jmrt.2025.02.184

[16] Fu, Y., Li, J., Luo, H., Du, C., & Li, X. (2021). Recent advances on environmental corrosion behavior and mechanism of high-entropy alloys. *Journal of Materials Science & Technology*, *80*, 217-233. https://doi.org/10.1016/j.jmst.2020.11.044

[17] Wang, Y., Li, G., Qi, H., Zhang, W., Chen, R., Su, R., Yu, B., & Qu, Y. (2024). Effect of non-metallic silicon content on the microstructure and corrosion behaviour of AlCoCrFeNi high-entropy alloys. *Materials Chemistry and Physics*, *315*, 128974. https://doi.org/10.1016/j.matchemphys.2024.128974

[18] Gu, X., Zhuang, Y., & Huang, D. (2022). Corrosion behaviors related to the microstructural evolutions of as-cast Al0. 3CoCrFeNi high entropy alloy with addition of Si and Ti elements. *Intermetallics*, *147*, 107600. https://doi.org/10.1016/j.intermet.2022.107600

[19] Yang, H., Liu, X., Li, A., Li, R., Xu, S., Zhang, M., Yu, P., Yu, S., Jiang, M., & Huo, C. (2023). Effect of silicon addition on the corrosion resistance of Al0. 2CoCrFe1. 5Ni high-entropy alloy in saline solution. *Journal of Alloys and Compounds*, *964*, 171226. https://doi.org/10.1016/j.jallcom.2023.171226

[20] Shi, X., Liang, H., & Li, Y. (2025). Effect of Si content on phase structure, microstructure, and corrosion resistance of FeCrNiAl0.7Cu0.3Six high-entropy alloys in 3.5% NaCl solution. *Coatings*, *15*(3), 342. https://doi.org/10.3390/coatings15030342